

Your dedication goes here

Table of Contents

Registration of histological serial sectionings <i>Jan Modersitzki¹, Oliver Schmitt², and Stefan Wirtz¹</i>	1
--	---

List of Contributors

Otmar Scherzer

University of Innsbruck
Institute of Computer Science
Technikerstraße 21a
6020 Innsbruck, Austria
otmar.scherzer@uibk.ac.at

Armin Schoisswohl

GE Medical Systems
Kretz Ultrasound
Tiefenbach 15
4871 Zipf, Austria
armin.schoisswohl@med.ge.com

Reto Bale

Universitätsklinik für Radiodiagnostik
SIP-Labor
Anichstraße 35
6020 Innsbruck, Austria
reto.bale@uibk.ac.at

Harald Grossauer

University of Innsbruck
Institute of Computer Science
Technikerstraße 21a
6020 Innsbruck, Austria
harald.grossauer@uibk.ac.at

Stefan Henn

Heinrich-Heine University of
Düsseldorf
Lehrstuhl für Mathematische Opti-
mierung
Mathematisches Institut
Universitätsstraße 1

40225 Düsseldorf, Germany
henn@am.uni-duesseldorf.de

Lars Hömke

Forschungszentrum Jülich GmbH
Institut für Medizin
Street No.
52425 Jülich, Germany
hoemke@am.uni-duesseldorf.de

Kristian Witsch

Heinrich-Heine University of
Düsseldorf
Lehrstuhl für Angewandte Mathematik
Mathematisches Institut
Universitätsstraße 1
40225 Düsseldorf, Germany
witsch@am.uni-duesseldorf.de

Stephen L. Keeling

Karl-Franzens University of Graz
Institute of Mathematics
Heinrichstraße 36
8010 Graz, Austria
stephen.keeling@uni-graz.ac.at*

Jan Modersitzki

University of Lübeck
Institute of Mathematics
Wallstraße 40
D-23560 Lübeck
modersitzki@math.uni-luebeck.de

Oliver Schmitt

University of Rostock

Institute of Anatomy
Gertrudenstraße 9
D-18055 Rostock, Germany
schmitt@med.uni-rostock.de

Stefan Wirtz
University of Lübeck
Institute of Mathematics
Wallstraße 40
D-23560 Lübeck
wirtz@math.uni-luebeck.de

Ulrich Clarenz
Gerhard-Mercator University of
Duisburg
Institute of Mathematics
Lotharstraße 63/65,
47048 Duisburg, Germany
clarenz@math.uni-duisburg.de

Marc Droske
Gerhard-Mercator University of
Duisburg
Institute of Mathematics
Lotharstraße 63/65,
47048 Duisburg, Germany
droske@math.uni-duisburg.de

Stefan Henn
Heinrich-Heine University of
Düsseldorf
Lehrstuhl für Mathematische Opti-
mierung
Universitätsstraße 1
40225 Düsseldorf, Germany
henn@am.uni-duesseldorf.de

Martin Rumpf
Gerhard-Mercator University of
Duisburg
Institute of Applied Mathematics
Lotharstraße 63/65,

47048 Duisburg, Germany
rumpf@math.uni-duisburg.de

Kristian Witsch
Heinrich-Heine University of
Düsseldorf
Lehrstuhl für Angewandte Mathematik
Universitätsstraße 1
40225 Düsseldorf, Germany
witsch@math.uni-duisburg.de

Joachim Weickert
Mathematical Image Analysis Group,
Faculty of Mathematics and Computer
Science,
Saarland University, Building 27,
66041 Saarbrücken, Germany.
weickert@mia.uni-saarland.de.

Andrés Bruhn
Mathematical Image Analysis Group,
Faculty of Mathematics and Computer
Science,
Saarland University, Building 27,
66041 Saarbrücken, Germany.
bruhn@mia.uni-saarland.de.

Nils Papenberg
Mathematical Image Analysis Group,
Faculty of Mathematics and Computer
Science,
Saarland University, Building 27,
66041 Saarbrücken, Germany.
papenberg@mia.uni-saarland.de.

Thomas Brox
Mathematical Image Analysis Group,
Faculty of Mathematics and Computer
Science,
Saarland University, Building 27,
66041 Saarbrücken, Germany.
brox@mia.uni-saarland.de.

Registration of histological serial sectionings

Jan Modersitzki¹, Oliver Schmitt², and Stefan Wirtz¹

¹ University of Lübeck
Institute of Mathematics
Wallstraße 40
D-23560 Lübeck
{modersitzki,wirtz}@math.uni-luebeck.de

²University of Rostock
Institute of Anatomy
Gertrudenstraße 9
D-18055 Rostock, Germany
schmitt@med.uni-rostock.de

Summary Image registration is a fundamental task in today's medical imaging. In particular for histological serial sectioning, where a three-dimensional object is cut into thin sections for a further microscopic analysis, registration leads to a three dimensional reconstruction of the sections. This reconstruction enables an exploration of the digitized data in any direction, not only in the cutting direction. In this paper, we describe cutting and reconstruction procedures. For the reconstruction, we use linear as well as non-linear registration schemes. Moreover, we present some results for a whole brain of a *Sprague Dawley* rat.

1 Introduction

Histological serial sectioning is a valuable and essential tool in visualizing microscopic structures of tissue like, for example, cells. A three-dimensional object is sectioned into thin (5–40 μm) sections; cf. Fig. 1. These sections form the basis for a microscopic investigation; cf. Fig. 2. It is important to note that the sections are inevitable to deduce information about cells like, for example, size, position and orientation. Alternative three-dimensional imaging devices like, for example, computer tomography (CT) or (micro) magnetic resonance imaging (MRI or μMRI) have resolutions that are far behind the visualization of cells [4, 11]. The information obtained from the microscopic analysis is related to the coordinates in the two-dimensional tissue section rather than the ones of the three-dimensional original object. However, the sectioning process introduces all kinds of deformations to the tissue and this results in distorted tissue sections; cf. Fig. 1(b). Therefore, the two-dimensional information can not be used to perform an overall three-dimensional analysis and visualization.

A remedy is provided by so-called image registration techniques; cf., e.g., [24, 17]. Image registration is one of the fundamental tasks in today's image processing and is used routinely in many medical applications; for an overview, see, e.g., [6,

16, 22, 17] and references therein. The objective of image registration is to make images which are taken at different times, from different perspectives, and/or from different devices to be more alike.

Particularly in the context of histological serial sectioning, the aim is to recover non-deformed versions of the tissue sections. Ideally, these non-deformed sections can then be glued together to get a three-dimensional tissue back; see also [19, 8, 21, 2]. By knowing the deformations, one can map from the deformed to the non-deformed tissue and vice versa. Therefore, one can also visualize cells in a three-dimensional view and perform a three-dimensional structure analysis.

Here, we describe a registration procedure for images arising in the Human NeuroScanning Project (HNSP) [23]. The overall goal of this project is a three-dimensional reconstruction of a whole human brain down to particular neurons based on microscopic modalities. This data will then be used as the basic structure for the integration of functional data based on stochastic mapping and later on for modelling and simulation studies in a virtual brain; see [23] for details.

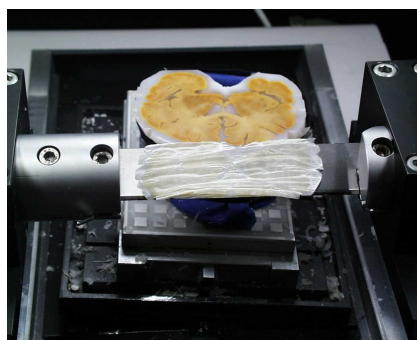
The production of the histological serial sectioning of a human brain is addressed in Section 2. As illustrated in Fig. 3, non-linear registration is essential for the reconstruction of the brain sections. Fig. 3(a,b) displays two flat bed scans of consecutive sections of a serial sectioning of a human brain. The scans have been pre-registered using a principal axis transformation; cf., e.g., [1]. As it is apparent from the difference image Fig. 3(c), intolerable differences with respect to the geometry are observable (particularly near the cerebral cortex). Fig. 3(d) shows the difference after an affine linear registration. Though the difference has been reduced considerably and especially with respect to the left hemisphere, the result is still not convincing since large deformations are observable (particularly in the right hemisphere). This example demonstrates that the deformations to be observed are in general non-linear and therefore non-linear registration techniques have to be used in addition. Fig. 3(e) finally displays the difference image after an additional so-called elastic registration of these two slices. For elastic registration, we refer to the extended literature; see, e.g., [5, 3, 7, 10, 9, 12, 17]

The remaining part of the paper is organized as follows. In Section 3 we describe the three phases of our registration scheme. The first phase is related to some preprocessing: digitizing the tissue sections, segmentation, principal axis transformation (PAT) based pre-registration of the images (cf., e.g., [1]), and gray value equalization. The second phase is an affine linear registration of the image stack and the last phase is an elastic registration thereof.

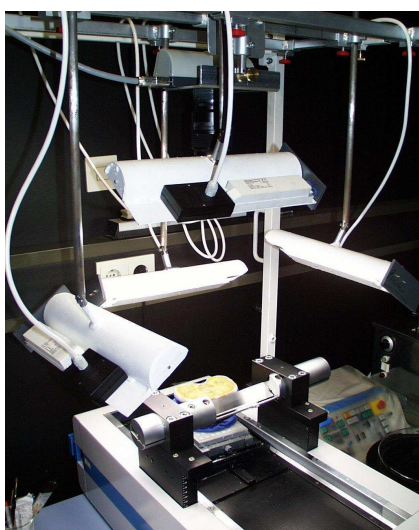
Section 4 presents some results, the reconstruction and visualization of a whole brain of a *Sprague Dawley* rat. Moreover, we also present some timings for these particular reconstructions. Finally, we conclude in Section 5 and comment on future work.



(a) paraffin embedded human brain (sagittal sectioning)



(b) sliding microtome with tissue section on the blade (axial sectioning)



(c) slicing workbench

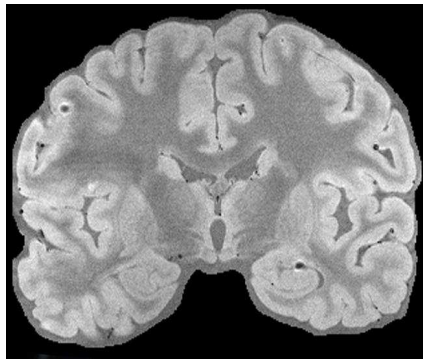


(d) high resolution FBS

Fig. 1. Sectioning machinery: (a) paraffin embed human brain; (b) sliding microtome with tissue section on top of the blade; (c) part of the slicing workbench; (d) transparent flat-bed-scanner (FBS) with microscopic slide.

2 Material

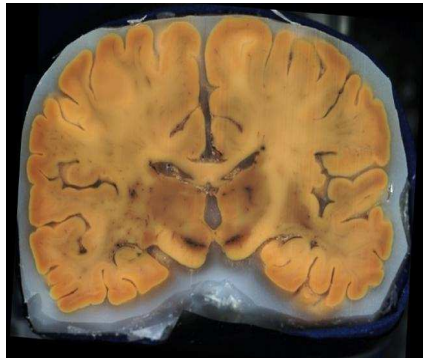
In order to locate the spatial positions of single neurons, the postmortem brain from a 55 year old male human voluntary donor was prepared in several steps; cf. [23]. In the beginning, the brain was fixed in a neutral buffered formaldehyde solution. After fixation an MR-scan of the brain was produced to obtain information of the original topology; cf. Fig. 2(a). Finally, the brain was dehydrated and embedded in paraffin; cf. Fig. 1(a).



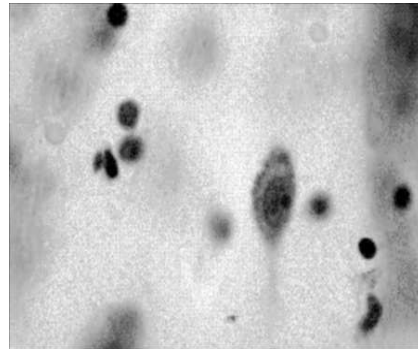
(a) slice of MRI scan



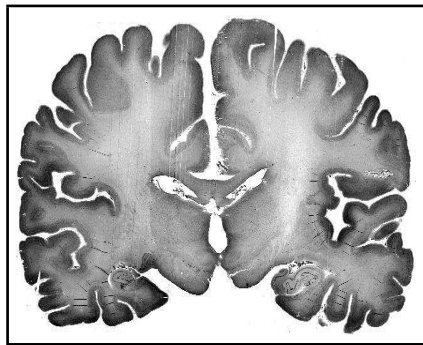
(b) light microscope



(c) episcopy image



(d) cells



(e) scan of histological section

Fig. 2. Different image modalities of the brain: (a) MRI slice, (c) episcopy image, (e) transparent flat bed scan of a microscopic slide; (b) light-microscope with microscopic slides on the table; (d) view through the microscope.

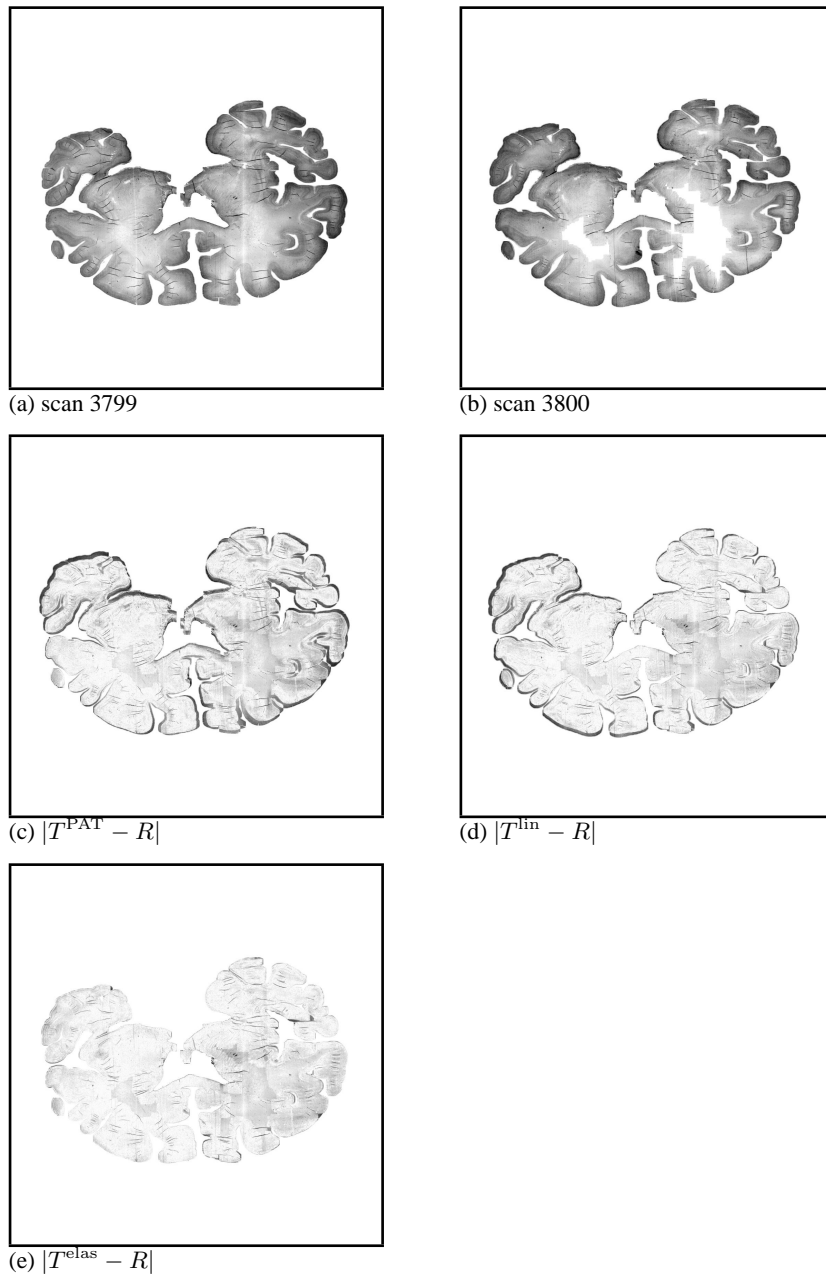


Fig. 3. Two consecutive axial scans 3799 (a) and 3800 (b) as well as difference images: (c) after PAT registration, (d) after optimal affine linear registration, and (e) after elastic registration.

This preparatory work was followed by sectioning the brain in $20\ \mu\text{m}$ thick slices (about 5000 for this brain) using a sliding microtome; cf. Fig. 1(b,c). A high resolution episcopic image (1352×1795 pixels, three colors) was taken before each slicing step; cf. Fig. 1(c) and Fig. 2(c).

Fig. 1(b) also displays a tissue slice after sectioning. The tissue slice was then stretched in warm water at 55°C for flattening. Thereafter, it was transferred onto a microscopic slide and dried. After drying, the sections were deparaffinized, stained in gallocyenin chromalum, and mounted under cover-glasses.

A specialized light microscope with an extraordinarily large object range of $250 \times 250\ \text{mm}^2$ is used to visualize all cells of the large tissue sections (Fig. 2(b,d)). Different neuronal entities were analyzed on different structural scales, i.e. from macroscopic details down to the cellular level; see [23] for the image processing. Although scanner technology has been improved tremendously within the last years, yet light-microscopy represents the only possibility to visualize fine details, like, for example, the exact spatial location of cells (Fig. 2(d)); cf. [23].

In order to relate the microscopic data to a macroscopic view of the slice and to recover the geometrical deformation of the tissue introduced by the various sectioning steps, flat bed scans of the slices were produced (Fig. 1(d) and Fig. 2(e)). These scans form the basis for our numerical treatment. Note, the fixed and mounted tissue sections can not be deformed whereas the scans (i.e. the digital images of the sections) can. Using a resolution of 2032 parts per inch in an 8 Bit gray-scale mode the digitized images range between 5000×2000 and 11000×7000 pixels (about 196 MBytes storage for the largest scan).

3 Registration procedures

In this section we describe our reconstruction procedure for a stack of n scans. We use a continuous image model which enables us to use fast numerical schemes like, for example, Gauss-Newton schemes.

In Section 3.1 we discuss the discretization and interpolation schemes. In Section 3.2 we describe our preprocessing. The main objective is a segmentation of the scan of the brain and a gray value homogenization. The latter is necessary because the staining of consecutive section shows large variations. Section 3.3 summarizes general remarks concerning the registration of a stack of preprocessed scans. The second phase of our reconstruction, which may also be viewed as a further preprocessing step, consists of an affine linear registration; cf. Section 3.4. Here, the transformation can be phrased in terms of a small number of parameters and we end up with a parametric registration problem. The third and final phase consists of an elastic registration; cf. Section 3.5. For the affine linear and elastic registration we exploit a multilevel approach; see also [13, 14]. Here, the smoothed images are down-sampled and registration results obtained on a coarse level are used as starting values for the registration on the next finer level.

3.1 Discretization

Though the scans of the sections present discrete data, we prefer a continuous image model. Using a continuous model, the numerical schemes become independent of the actual image resolution and, most importantly, we are able to apply fast optimization schemes which typically rely on at least first order derivatives. However, for two reasons we ignore the need of differentiability of the transformed images and use a bilinear interpolation scheme, only. One reason is that higher order interpolation schemes, like, e.g. B-spline interpolations lead to oscillations and Gibbs phenomenon which are very pronounced at the cerebral cortex, of course. The second reason is that our numerical experiments strongly indicates that the benefit of higher order interpolation is hardly noticeable but the price in terms of computing time is quite high.

We assume all discrete data to be of the size m -by- n . The images are interpolated at pixel values (i, j) which are associated to points $(i/(m + 1), j/(n + 1)) \in \Omega :=]0, 1[{}^2$. For an arbitrary point (x, y) we set $T(x, y) = b$, if $(x, y) \notin \Omega$. Here, b is the gray value of the background which is typically zero. For the evaluation of $T(x, y)$, where $(x, y) \in \Omega$, we use a bilinear interpolation scheme based on the four closest pixels. Spatial derivatives are computed using central differences of the pre-smoothed image, where a convolution with a discrete Gaussian kernel is used for smoothing. For the computation of the two-dimensional integrals we use the midpoint quadrature rule.

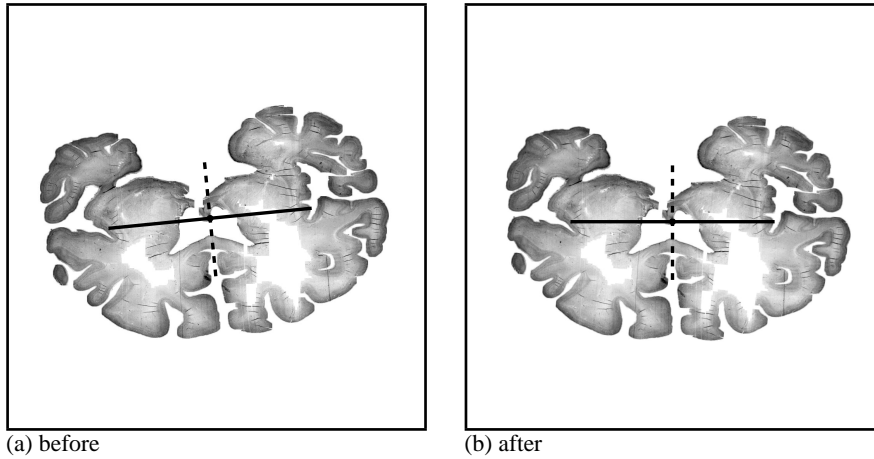


Fig. 4. Scan before (a) and after (b) pre-registration. The solid and dashed lines illustrate the first and second principal axis, respectively. The cross point is the center of gravity and the lengths indicate the standard deviations in principal directions.

3.2 Preprocessing

The stack of scans $S^{(j)}$, $j = 1, \dots, n$, forms the basis for our numerical treatment. In a preprocessing step, each image is segmented using a simple but robust threshold based algorithm and it can be normalized using a PAT; cf., e.g., [1, 17].

Fig. 4 illustrates the normalization procedure for scan $S^{(3800)}$ of a human brain. The solid and dashed lines illustrate the first and second principal axis, respectively. The cross point is the center of gravity and the lengths of the lines indicate the standard deviations in the principal directions. Note that the PAT registration is redundant. Moreover, particularly for scans resulting from corrupted sections, we observed that a PAT normalization can lead to an inferior starting point.

Before registration we apply a gray value homogenization. We use the gray value statistic to equalize the gray value variation of the image stack which are due to staining variations. Let γ and σ denote the mean gray value and its standard deviation with respect to the non-zero image, respectively. With $\hat{\gamma}$ and $\hat{\sigma}$ we denote the target values obtained from a sliding median filtering of the corresponding values of the image stack. We replace the image S by $\hat{S} := \frac{\hat{\sigma}}{\sigma}(S - \gamma) + \hat{\gamma}$, where clipping is applied to out of range values. Hence, by linearity of the expectation value we have

$$\mathbb{E}[\hat{S}] = \frac{\hat{\sigma}}{\sigma}\mathbb{E}[S - \gamma] + \hat{\gamma} = \hat{\gamma} \quad \text{and} \quad \mathbb{E}[(\hat{S} - \hat{\gamma})^2] = \left(\frac{\hat{\sigma}}{\sigma}\right)^2\mathbb{E}[(S - \gamma)^2] = \hat{\sigma}^2.$$

To minimize notational overhead, we subsequently denote the normalized scans also by $S^{(j)}$.

3.3 Stack registration

Our registration is based on the L_2 -difference or Sum of Squared Differences (SSD) (cf., e.g., [6])

$$D(A, B) := \frac{1}{2} \int_{\Omega} (A(x) - B(x))^2 d\mathbf{x}, \quad (1)$$

where A, B are two given images. For any image $S^{(j)}$ we consider an individual transformation $\mathbf{u}^{(j)}$, such that the joint distance

$$\begin{aligned} J(\mathbf{u}^{(1)}, \dots, \mathbf{u}^{(n)}) &:= \sum_{j=2}^n D(S^{(j-1)} \circ \mathbf{u}^{(j-1)}, S^{(j)} \circ \mathbf{u}^{(j)}) \\ &= \frac{1}{2} \sum_{j=2}^n \int_{\Omega} (S^{(j-1)} \circ \mathbf{u}^{(j-1)} - S^{(j)} \circ \mathbf{u}^{(j)})^2 dx \end{aligned} \quad (2)$$

becomes minimal, where $(S^{(j)} \circ \mathbf{u}^{(j)})(\mathbf{x}) := S^{(j)}(\mathbf{u}^{(j)}(\mathbf{x}))$ denotes the transformed scan.

In order to avoid systematic scaling errors in the registration of the stack, the image $S^{(\nu)}$ with largest number of non-zero pixels remains unaltered throughout the registration, i.e. $\mathbf{u}^{(\nu)}(\mathbf{x}) = \mathbf{x}$. Therefore, the above minimization problem (2)

decouples into two parts. Moreover, for the linear registration part, we constrain the transformations $\mathbf{u}^{(e)}$, $e = 1, n$, to be volume preserving, i.e.,

$$\det \nabla \mathbf{u}^{(e)} = 1. \quad (3)$$

Since a re-scaling of the images $S^{(e)}$ is already penalized by the elastic regularizer, we do not constrain $\mathbf{u}^{(e)}$ in the non-linear registration.

The constraints on $\mathbf{u}^{(e)}$ to be volume preserving is crucial, particularly when registering cone shaped objects. Without these additional constraints, one may obtain a cylinder shaped result. However, not all shape problems can be cured by this approach. Fig. 5 displays two three dimensional objects, a box and a twisted copy. If we would produce coronal serial sectioning, we would obtain the same images for both objects; cf. Fig. 5(c). Therefore one has to face ambiguity in the reconstruction of three-dimensional objects from two-dimensional slices.

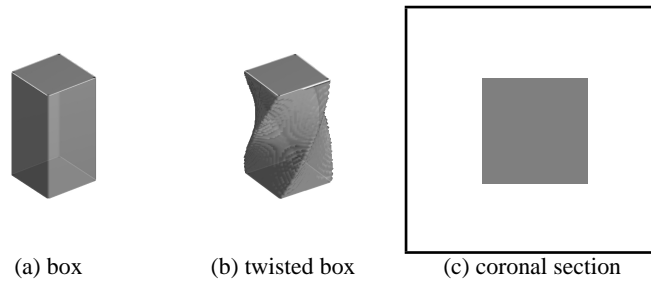


Fig. 5. Two three-dimensional objects, a box (a) and a twisted copy (b); arbitrary non-empty axial section through either of the two objects (c).

It is important to note that the registration discussed here aims to recover fine level details. Registration can not compensate for global shape variations, which are already introduced by removing the brain from the skull or by putting it onto a table. In order to correct for these global shape deformations, additional information has to be supplied. We will use an a priori taken magnetic resonance scan (MRI) of the brain (Fig. 2(a)) as a non-deformed reference and finally register our reconstruction to the MRI.

In the above discussion we assumed that the scan with maximal number of non-zero pixels is uniquely defined. However, the approach can be extended easily to the case when more than one scan take the maximum. As a matter of fact, we never observed this situation in our numerical experiments.

For the numerical minimization of J in (2), we use an iterative multilevel non-linear block Gauss-Seidel scheme. The iteration counter is denoted by k . For $k = 0$, we set $\mathbf{u}_k^{(j)}$ such that the associated map becomes the identity, $\mathbf{u}_k^{(j)}(\mathbf{x}) = \mathbf{x}$, $j = 1, \dots, n$. For $j = 1, \dots, n$, $j \neq \nu$, we minimize

$$\hat{J}_j(\mathbf{u}^{(j)}) := J(\mathbf{u}_{k+1}^{(1)}, \dots, \mathbf{u}_{k+1}^{(j-1)}, \mathbf{u}^{(j)}, \mathbf{u}_k^{(j+1)}, \dots, \mathbf{u}_k^{(n)}), \quad (4)$$

with respect to $\mathbf{u}^{(j)}$ only and the minimizer is denoted by $\mathbf{u}_{k+1}^{(j)}$. Setting $k \mapsto k + 1$ we repeat the iteration until stagnation in the distance measure J is observed.

Of course, other optimization strategies can be used as well. However, a discussion is beyond the scope of this paper and we therefore refer to the optimization literature; see, e.g., [18] and references therein.

Note that the minimization in (4) is only with respect to $\mathbf{u}^{(j)}$. With $\hat{S}_k^{(j)}$ denoting the deformed image, $\hat{S}_k^{(j)}(\mathbf{x}) = S^{(j)}(\mathbf{u}_k^{(j)}(\mathbf{x}))$ and some constants d we have

$$\begin{aligned} \hat{J}_1(\mathbf{u}^{(1)}) &= D(S^{(1)} \circ \mathbf{u}^{(1)}, \hat{S}_k^{(2)}) + d, \\ \hat{J}_n(\mathbf{u}^{(n)}) &= D(S^{(n)} \circ \mathbf{u}^{(n)}, \hat{S}_k^{(n-1)}) + d, \\ \hat{J}_j(\mathbf{u}^{(j)}) &= D(\hat{S}_{k+1}^{(j-1)}, S^{(j)} \circ \mathbf{u}^{(j)}) + D(S^{(j)} \circ \mathbf{u}^{(j)}, \hat{S}_k^{(j+1)}) + d_1 \\ &= D(S^{(j)} \circ \mathbf{u}^{(j)}, \frac{1}{2}\hat{S}_{k+1}^{(j-1)} + \frac{1}{2}\hat{S}_k^{(j+1)}) + d_2. \end{aligned}$$

Therefore, a minimizer of (4) can be obtained by minimizing

$$J_2(\mathbf{u}) := D(R, T \circ \mathbf{u}), \quad (5)$$

where

$$T := S^{(j)} \quad \text{and} \quad R := \begin{cases} \frac{1}{2}(\hat{S}_{k+1}^{(j-1)} + \hat{S}_k^{(j+1)}), & 1 < j < n, \\ \hat{S}_k^{(2)}, & j = 1, \\ \hat{S}_k^{(n-1)}, & j = n. \end{cases}$$

As already pointed out, we apply a multilevel approach for the minimization of (5). The images on the fine grid are smoothed by convolving with a discrete Gaussian kernel and are down-sampled to a coarse grid. The registration results on the coarse grid are mapped to the fine grid and serve as generally excellent starting values for the registration on the fine grid.

3.4 Affine linear registration

Since an affine linear transformation \mathbf{u} belongs to a finite dimensional space, it can be parameterized like, for example,

$$\mathbf{u}(\mathbf{x}) := \begin{pmatrix} u_1 x_1 + u_2 x_2 + u_3 \\ u_4 x_1 + u_5 x_2 + u_6 \end{pmatrix} \quad (6)$$

and we therefore associate \mathbf{u} with the parameter vector (u_1, \dots, u_6) . For the volume preserving map we use the parameterization

$$\mathbf{u}^{(e)}(\mathbf{x}) = \begin{pmatrix} 1 & u_1^{(e)} \\ 0 & 1 \end{pmatrix} \begin{pmatrix} \cos u_2^{(e)} & -\sin u_2^{(e)} \\ \sin u_2^{(e)} & \cos u_2^{(e)} \end{pmatrix} \begin{pmatrix} x_1 \\ x_2 \end{pmatrix} + \begin{pmatrix} u_3^{(e)} \\ u_4^{(e)} \end{pmatrix},$$

where the first matrix describes shear and the second rotation.

For a numerical solution of (5) we exploit a Gauss-Newton scheme, where only first order derivatives of the images are needed; cf., e.g., [18]. Starting with an initial guess \mathbf{u}_0 , we obtain $\mathbf{u}_{k+1} = \mathbf{u}_k + \delta\mathbf{u}$, where $\delta\mathbf{u}$ is the solution of the linearized L_2 approximation problem

$$\|R - T \circ \mathbf{u}_{k+1}\| \approx \|R - T \circ \mathbf{u}_k - \nabla_{\mathbf{u}}[T \circ \mathbf{u}]_{\mathbf{u}=\mathbf{u}_k} \delta\mathbf{u}\| = \min.$$

The generic derivative $\nabla_{\mathbf{u}}[T \circ \mathbf{u}]$ is given by

$$\begin{aligned} \partial_{u_1}[T \circ \mathbf{u}] &= \partial_1 T \cdot x_1, & \partial_{u_4}[T \circ \mathbf{u}] &= \partial_2 T \cdot x_1, \\ \partial_{u_2}[T \circ \mathbf{u}] &= \partial_1 T \cdot x_2, & \partial_{u_5}[T \circ \mathbf{u}] &= \partial_2 T \cdot x_2, \\ \partial_{u_3}[T \circ \mathbf{u}] &= \partial_1 T, & \partial_{u_6}[T \circ \mathbf{u}] &= \partial_2 T, \end{aligned}$$

where the directional derivatives $\partial_j T = \partial_j T(\mathbf{u}(\mathbf{x}))$ are approximated by centered finite difference approximation of the smoothed images T ; cf. Section 3.1. The derivatives for the first and last section are given by

$$\begin{aligned} \partial_{u_1^{(e)}}[T \circ \mathbf{u}^{(e)}] &= \partial_1 T \cdot (sx_1 + cx_2), \\ \partial_{u_2^{(e)}}[T \circ \mathbf{u}^{(e)}] &= \partial_1 T \cdot ((ca - s)x_1 - (c + as)x_2) - \partial_2 T(-cx_1 + sx_2), \\ \partial_{u_3^{(e)}}[T \circ \mathbf{u}^{(e)}] &= \partial_1 T, & \partial_{u_4^{(e)}}[T \circ \mathbf{u}^{(e)}] &= \partial_2 T. \end{aligned}$$

3.5 Elastic registration

As it is apparent from Fig. 3(d), an affine linear registration alone does not lead to satisfying reconstruction results. Therefore, a non-linear registration becomes necessary. Here, we use an elastic registration which has been studied for over 20 years; see, e.g., [5, 3, 7, 10, 17].

The basic idea of elastic registration can be described as follows. Assume that the template image has been painted onto a rubber. A deformation of the rubber results in a deformed template image but also introduces a potential energy to the rubber. The stronger the deformation the higher this potential becomes. The idea is to find a deformation which minimizes both, the distance between reference and deformed template as well as the elastic potential. Therefore, deformations leading to a very high elastic potential become disregarded even if they lead to small values of D . In other words, the distance measure (5) is regularized by the elastic potential and the registration problem becomes

$$J_{elas}(\mathbf{u}) = D(R, T \circ \mathbf{u}) + S(\mathbf{u}) = \min, \quad (7)$$

where

$$S(\mathbf{u}) = \int_{\mathbb{R}^2} \frac{\lambda}{2} (\operatorname{div} \mathbf{u})^2 + \mu \left\{ (\partial_1 u_1)^2 + (\partial_2 u_2)^2 + \frac{1}{2} (\partial_1 u_2 + \partial_2 u_1)^2 \right\} dx \quad (8)$$

and μ and λ are the so-called Lamé constants reflecting material properties; see, e.g., [17] for details.

This particular regularization in our registration scheme is motivated by the fact that the histological sections originally consist of almost pure paraffin wax. The deformation process due to sectioning is therefore expected to be dominated by the elastic properties of the section. Note that also other processes like, e.g., drying or mounting contributes to the overall deformations.

Note that in contrast to the affine linear registration where \mathbf{u} is described in terms of at most six parameters, the deformation in the continuous formulation of the nonlinear registration is not restricted to a finite dimensional search space. However, in our implementation we use a discretization where values of $\mathbf{u}(\mathbf{x})$ are computed for each pixel \mathbf{x} .

Following [9], a minimizer is characterized by the Euler-Lagrange equations

$$\mathcal{A}\mathbf{u}(\mathbf{x}) + \mathbf{f}(\mathbf{x}, \mathbf{u}(\mathbf{x})) = 0 \quad \text{for all } \mathbf{x} \in \Omega, \quad (9)$$

where the well-known Navier-Lamé operator \mathcal{A} is related to the Gâteaux-derivative of \mathcal{S} ,

$$\begin{aligned} \mathcal{A}[\mathbf{u}] &= \mu \Delta \mathbf{u} + (\lambda + \mu) \nabla \operatorname{div} \mathbf{u} \\ &= \mu \begin{pmatrix} \partial_{1,1} u_1 + \partial_{2,2} u_1 \\ \partial_{1,1} u_2 + \partial_{2,2} u_2 \end{pmatrix} + (\lambda + \mu) \begin{pmatrix} \partial_{1,1} u_1 \partial_{1,2} + u_2 \\ \partial_{1,2} u_1 \partial_{2,2} + u_2 \end{pmatrix} \end{aligned}$$

and the so-called force \mathbf{f} is related to the Gâteaux-derivative of \mathcal{D} ,

$$\mathbf{f}(\mathbf{x}, \mathbf{u}(\mathbf{x})) = \left(R(\mathbf{x}) - T(\mathbf{x} + \mathbf{u}(\mathbf{x})) \right) \cdot \nabla T(\mathbf{x} + \mathbf{u}(\mathbf{x})). \quad (10)$$

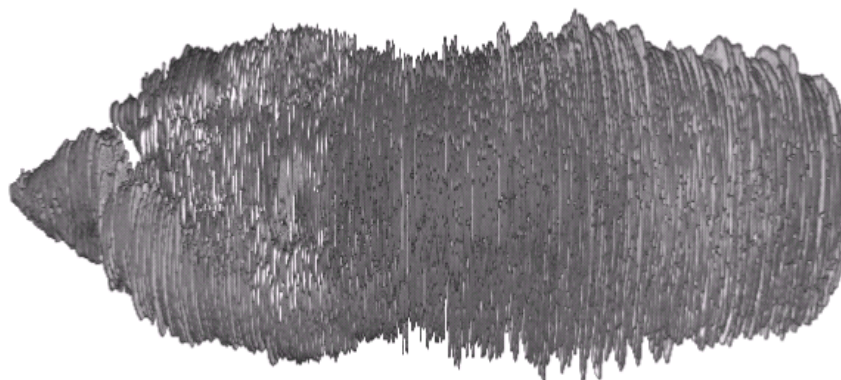
For the computation of a numerical solution, we used the scheme proposed in [9].

4 Results

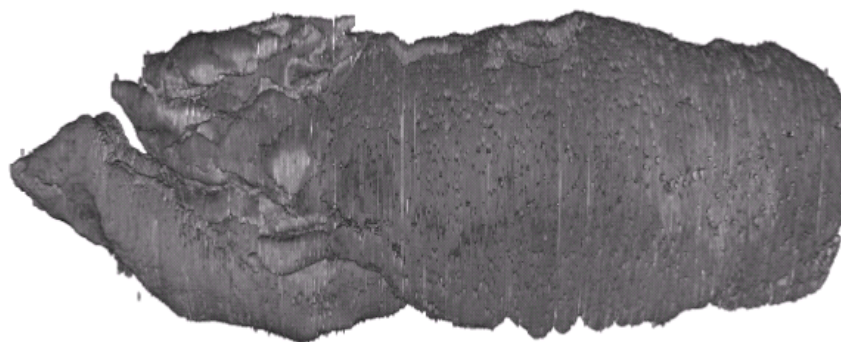
Fig. 6 displays some results for the registration of a stack of $n = 503$ slices from a *Sprague Dawley* rat brain. Each scan has a resolution of 1900×1900 pixels, which ends up in a total amount of 1.7 gigabytes (GB) of data. Heavily corrupted tissue sections were automatically detected and disregarded, such that 474 scans (1.6 GB) remained.

Fig. 6(a) displays a view of the non-registered stack and (b) a view of the elastically registered stack. To illustrate the value of the reconstruction, we resampled the data orthogonally to the direction of sectioning and show a virtual sagittal slice; see Fig. 7.

In the virtual sagittal slice structures like, for example, the cerebellar fissures, molecular and granular layer, and white substance of cerebellum are clearly recognizable. Note that the initial fuzzy looking brain now offers morphological details and obviously dramatic increase of surface smoothness. Overall, the displaced areas



(a) no registration



(b) elastic registration

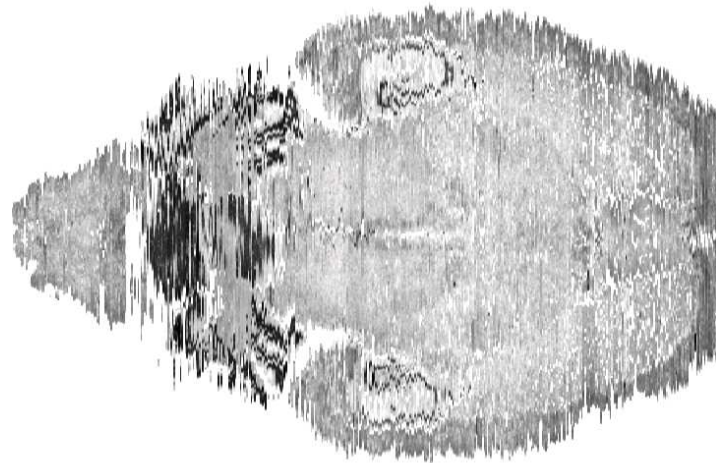
Fig. 6. Lateral view of the three-dimensional reconstruction of a whole rat brain; (a) no registration and (b) elastic registration.

are coherent again. It should be noted, that the registration is an indispensable technique for recognition, discussion and three-dimensional measurement of internal and external morphologic entities.

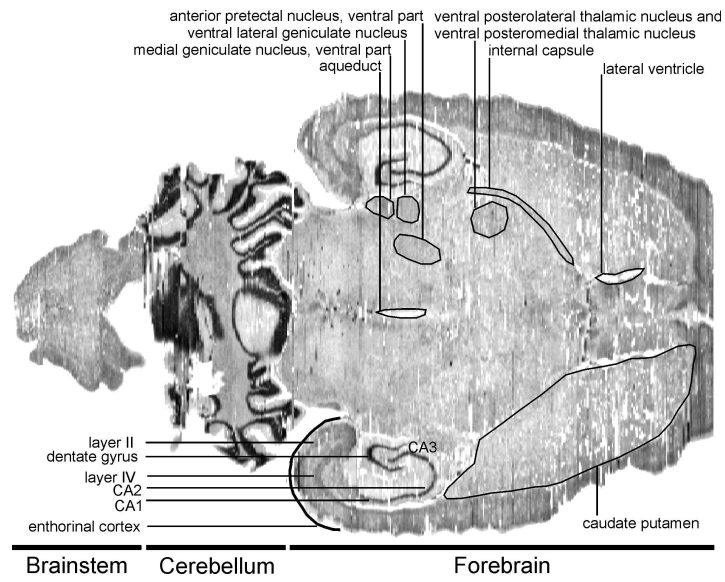
For this reconstruction, a linear pre-registration based on the principle axis transformation was performed. The error (cf. (2)) decreased by about 27%, i.e.

$$J(\mathbf{u}_{\text{PAT}}) \approx 0.73 \cdot J(\mathbf{u}_0).$$

For this reconstruction, it turned out that a pure elastic registration through five levels of a Gaussian pyramid (coarsest images 128×128 pixels) leads to a satisfying convergence. No PAT pre-registration was applied. The MATLAB [15] implemented



(a) no registration



(b) elastic registration

Fig. 7. Reproduced virtual slice (sagittal, orthogonal to the sectioning direction, Bregma - 5.82 mm, Interaural 4.18 mm; see, e.g., Paxinos & Watson [20]). A column of the virtual slice represents the intersection of the virtual slice with an original slice (axial); (a) no registration, (b) after elastic registration. Note that registration enables the identification of anatomical structure.

registration algorithm lasted about ten hours for the high-resolution images on a AMD Athlon XP 2700+, 1GB RAM, running Linux.

Only 35 iteration steps were needed and the error decreased by 79%, i.e.

$$J(\mathbf{u}_{elas}) \approx 0.21 \cdot J(\mathbf{u}_0).$$

In Tab. 1 the runtime results for the registration of images in different resolutions is assembled.

Table 1. Computational costs of the registration versus data dimensions; MB gives the storage requirements of the data, #levels the number of levels used in our multiscale approach, t_{iter} is the CPU time in minutes needed for one iteration on the finest grid, t_{total} is the total CPU time needed for the registration, and #iter is the overall number of iterations on all levels. The whole reconstruction process takes about ten hours CPU time using MATLAB [15] on a AMD Athlon XP 2700+, 1GB RAM, running Linux.

data dimensions	MB	#levels	t_{iter} (min)	t_{total} (min)	#iter
$128 \times 128 \times 474$	8	1	0.5	9	19
$256 \times 256 \times 474$	30	2	1.9	32	24
$512 \times 512 \times 474$	119	3	10.7	125	28
$1024 \times 1024 \times 474$	474	4	42.9	240	32
$1900 \times 1900 \times 474$	1632	5	149.5	547	35

Beside measuring the registration results with the distance measure \mathcal{D} , the results were evaluated by an anatomist. An important criterium is the improvement of the representation of small structures (subcortical nuclei, cortical areas) and the smoothness of inner and outer borders. The registered slices do fulfill this requirement. Generally, three classes of neuroanatomical structures are recognizable only after registration: 1) subcortical nuclei, 2) ventricles, and 3) certain cerebral and cerebellar cytoarchitectonic layers. More precisely, subcortical nuclei like the caudate putamen complex, medial geniculate nucleus - ventral part, anterior pretectal nucleus - ventral part, ventral posterolateral thalamic nucleus, ventral posteromedial thalamic nucleus among other things can be localized. Furthermore, the lateral ventricle and the aqueduct become visible. Finally, cytoarchitectonic layering at certain parts of the cerebral and the cerebellar cortex can be detected. In the forebrain one can observe hippocampal substructures like the CA1, CA2, CA3 regions (CA: cornu amonis) and the dentate gyrus, see Fig. 7. Moreover, in the entorhinal region the layer II (external granular layer) and IV (internal granular layer) are distinguishable.

In Fig. 8 the results of the registration processes are visualized in detail for a part of the rat brain. Fig. 8 depicts the three-dimensional reconstruction of 68 slices before (a) and after (b) registration. The massively shifted images yield to a blurred reconstruction without recognizable fine anatomic details (Fig. 8(c)). Fig. 8 also illustrates the variation of the internal structures before (c) and after (d) registration

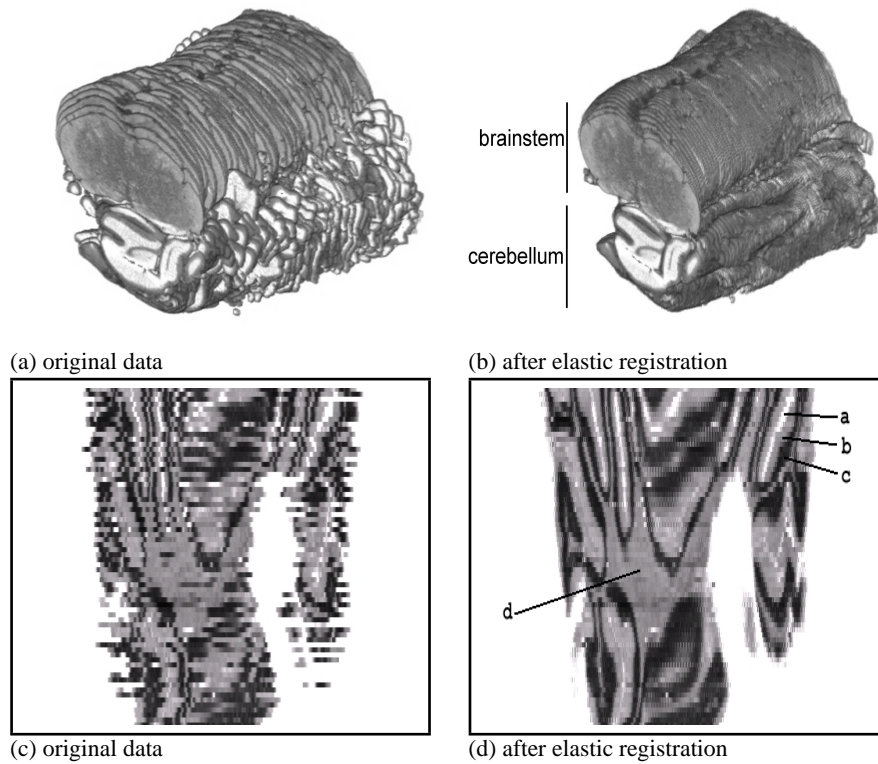


Fig. 8. Three-dimensional lateral view of a part of the rat brain and virtual orthogonal slices; (a) original data, (b) after elastic registration. This part of the brain shows the brainstem at the top and the cerebellum with folia at the bottom. The virtual slices (orthogonal to the sectioning direction) demonstrate the morphologic effect of registration: (c) original data, (d) after elastic registration. Recognizable structures after registration: a cerebellar fissures, b molecular layer, c granular layer, d white substance of the cerebellum.

by means of virtual slice orthogonal to the sectioning direction. Note, that the registration results allows for a detailed discussion of the internal structures.

5 Conclusions

We presented the first fully reconstructed rat brain at a resolution at level of the micrometer scale. The huge amount of data (≈ 1.6 GB) as well as the required quality demand for a special registration technique. Only the use of a specific variational technique accompanied by strategies to incorporate special properties of the underlying tissue enables us to match the high anatomical demands.

The backbone of the scheme is a super-fast solution technique for the inner linear system. This technique is accompanied by sound strategies for accelerating the outer

iteration. This includes a multi-scale approach based on a Gaussian pyramid as well as a sophisticated estimation of the material constants for the elastic potential.

The results of the registration process enable the identification of histological details that pertain to three distinct groups of neuroanatomical structures: subcortical nuclei, ventricles and cerebellar or cerebral cytoarchitectonic layers. Before registration the detection of these structures was impossible. Therefore, it is essential to apply elastic registration to this kind of non-linear problem. Furthermore, now it is feasible to develop strategies for three-dimensional morphometric analysis of specific areas in registered stacks of images derived from normal and pathologic brains for experimental studies. Finally, the obvious advantages were quantified by a distance measure leading to an improvement of about 79% after just 35 iteration steps.

Currently we are working at a full reconstruction of a human brain. Here the task is to align about 6000 slices of dimension (12000×7000) pixels (resolution: $31.75\mu\text{m}$ per pixel)! Preliminary results look very promising and indicate that the outlined approach is capable of dealing with such an amount of data on a PC from the shelf.

References

1. N. M. Alpert, J. F. Bradshaw, D. Kennedy and J. A. Correia: The principal axes transformation – A method for image registration, *Journal of nuclear medicine* **31/10**, pp 1717-1722, (1990)
2. V. Arsigny, X. Pennec and N. Ayache: A novel family of geometrical transformations: Polyrigid transformations. application to the registration of histological slices, Research report 4837, INRIA, (2003)
3. R. Bajcsy and S. Kovačič: Toward an individualized brain atlas elastic matching, Tech. Report MS-CIS-86-71 Grasp Lap 76, Dept. of Computer and Information Science, Moore School, University of Philadelphia, (1986)
4. H. Benveniste and S. Blackland: MR microscopy and high resolution small animal mri: applications in neuroscience research, *Progress in Neurobiology*, **67**, pp 393-420, (2002)
5. C. Broit: Optimal registration of deformed images, Ph.D. thesis, Computer and Information Science, University of Pennsylvania, (1981)
6. L. G. Brown: A survey of image registration techniques, *ACM Computing Surveys*, **24/4**, pp 325-376, (1992)
7. G. E. Christensen: Deformable shape models for anatomy, Ph.D. thesis, Sever Institute of Technology, Washington University, (1994)
8. T. Delzescaux, J. Dauguet, F. Condé, R. Maroy and V. Frouin: Using 3d non rigid FFD-based method to register post mortem 3d histological data and in vivo MRI of a baboon brain, MICCAI 2003 (R. E. Ellis and T. M. Peters (Eds.), LNCS, Springer, **2879**, pp 965-966, (2003)
9. B. Fischer and J. Modersitzki: Fast inversion of matrices arising in image processing, *Num. Algo.* **22**, pp 1-11 (1999)
10. J. C. Gee, D. R. Haynor, L. Le Briquer and R. Bajcsy: Advances in elastic matching theory and its implementation, *CVRMed*, pp 63-72, (1997)

11. S. C. Grant, D. L. Buckley, S. Gibbs, A. G. Web and S. J. Blackland: Mr microscopy of multicomponent diffusion in single neurons, *Magnetic Resonance in Medicine* **46**, pp 1107-1112, (2001)
12. S. Henn and K. Witsch: Iterative multigrid regularization techniques for image matching, *SIAM J. on Scientific Comp.* **23/4**, pp 1077-1093, (2001)
13. B. Jähne: *Digital image processing*, 4th ed., Springer, (1997)
14. J. Kybic and M. Unser: Multidimensional elastic registration of images using splines, *ICIP in Vancouver*, 10.-13.09.2000, pp 1-4, (September 2000)
15. MathWorks, Natick, Mass.: *Matlab user's guide*, (1992)
16. C. R. Maurer and J. M. Fitzpatrick: *Interactive image-guided neurosurgery*, ch. A Review of Medical Image Registration, pp. 17-44, Park Ridge, IL, American Association of Neurological Surgeons, (1993)
17. J. Modersitzki: *Numerical methods for image registration*, Oxford University Press, (2004)
18. J. Nocedal and S. J. Wright: *Numerical optimization*, Springer, New York (1999)
19. S. Ourselin, A. Roche, G. Subsol, X. Pennec and C. Sottonnet: Automatic alignment of histological sections for 3D reconstruction and analysis, *Tech. Report 3595*, Institut National de Recherche en Informatique et en Automatique, France, (Dec. 1998)
20. G. Paxinos C. and Watson: *The rat brain in stereotaxic coordinates*, 4th ed., Academic Press, (1998)
21. A. Pitiot, G. Malandain, E. Bardinet and P. Thompson: Piecewise Affine Registration of Biological Images, *WBIR 2003* (Gee, J.C. and Maintz, J.B.A. and Vannier, M.W. - Eds.), LNCS, **2717**, Springer, pp 91-101, (2003)
22. K. Rohr: *Landmark-based image analysis*, *Computational Imaging and Vision*, Kluwer Academic Publishers, Dordrecht, (2001)
23. O. Schmitt: *Die multimodale Architektonik des menschlichen Gehirns*, Habilitation, Institute of Anatomy, Medical University of Lübeck, Germany, (2001)
24. A. W. Toga and J. C. Mazziotta: *Brain mapping: The methods*, 2nd ed., Academic Press, (2002)